High-finesse Fabry-Perot cavities with bidimensional Si3N4 photonic-crystal slabs

X. Chen, C. Chardin, Kevin Makles, Charles Caër, Sheon Chua, Rémy Braive, Isabelle Philip, Tristan Briant, Pierre-François Cohadon, Antoine Heidmann, et al.

To cite this version:

X. Chen, C. Chardin, Kevin Makles, Charles Caër, Sheon Chua, et al.. High-finesse Fabry-Perot cavities with bidimensional Si3N4 photonic-crystal slabs. Light: Science and Applications, 2017, 6, pp.e16186. 10.1038/lsa.2016.190 . hal-01670338

HAL Id: hal-01670338
https://hal.science/hal-01670338v1

Submitted on 6 Jan 2025

Light: Science & Applications (2017) 6, e16190; doi:10.1038/lsa.2016.190
Official journal of the CIOMP 2047-7538/17
www.nature.com/lsa

ORIGINAL ARTICLE

High-finesse Fabry–Perot cavities with bidimensional Si_3N_4 photonic-crystal slabs

Xu Chen[1], Clément Chardin[1], Kevin Makles[1], Charles Caër[1,2], Sheon Chua[1], Rémy Braive[3,4], Isabelle Robert-Philip[3], Tristan Briant[1], Pierre-François Cohadon[1], Antoine Heidmann[1], Thibaut Jacqmin[1] and Samuel Deléglise[1]

Light scattering by a two-dimensional photonic-crystal slab (PCS) can result in marked interference effects associated with Fano resonances. Such devices offer appealing alternatives to distributed Bragg reflectors and filters for various applications, such as optical wavelength and polarization filters, reflectors, semiconductor lasers, photodetectors, bio-sensors and non-linear optical components. Suspended PCS also have natural applications in the field of optomechanics, where the mechanical modes of a suspended slab interact via radiation pressure with the optical field of a high-finesse cavity. The reflectivity and transmission properties of a defect-free suspended PCS around normal incidence can be used to couple out-of-plane mechanical modes to an optical field by integrating it in a free-space cavity. Here we demonstrate the successful implementation of a PCS reflector on a high-tensile stress Si_3N_4 nanomembrane. We illustrate the physical process underlying the high reflectivity by measuring the photonic-crystal band diagram. Moreover, we introduce a clear theoretical description of the membrane scattering properties in the presence of optical losses. By embedding the PCS inside a high-finesse cavity, we fully characterize its optical properties. The spectrally, angular- and polarization-resolved measurements demonstrate the wide tunability of the membrane's reflectivity, from nearly 0 to 99.9470 ± 0.0025%, and show that material absorption is not the main source of optical loss. Moreover, the cavity storage time demonstrated in this work exceeds the mechanical period of low-order mechanical drum modes. This so-called resolved-sideband condition is a prerequisite to achieve quantum control of the mechanical resonator with light.

Light: Science & Applications (2017) **6,** e16190; doi:10.1038/lsa.2016.190; published online 13 January 2017

Keywords: Fano resonance; high-reflectivity membrane; low-loss optical reflector; nanomembrane resonator; photonic-crystal slab; quantum optomechanics

INTRODUCTION

Fano resonances resulting from the interference between a discrete resonance and a broadband continuum of states are ubiquitous in physical science and constitute a unique resource in the field of nanophotonics[1]. The scattering properties of subwavelength periodic structures can be tailored by engineering their asymmetric Fano lineshapes. These extraordinary and controllable optical properties hold great promise in the context of nanophotonics, where fully integrated photonic-crystal slabs (PCS) can replace traditional Bragg multi-layers for various optical components. This approach has been successfully implemented in the context of optical filters[2], switches[3], sensors[4], lasers[5], detectors[6], slow-light and non-linear devices[7]. It has also been proposed as a possible route to reduce thermal noise in the mirrors of large-scale gravitational-wave interferometers[8].

Moreover, nanophotonics is playing an increasing role in the field of optomechanics by allowing sub-micron-scale mechanical resonators to interact via radiation pressure with highly confined optical fields. A very successful approach consists in co-localizing a photonic and a phononic mode in the small volume of a defect cavity in the plane of a PCS[9,10]. In this setup, the mechanical resonator consists of a GHz internal vibrational mode localized in a very small mode volume around the defect cavity. More recently, defect-free suspended PCSs have been used as lightweight mirrors of sub-micron thickness[11–13]. The out-of-plane vibrational modes of the membrane can be coupled to an optical field by integrating the membrane inside a high-finesse cavity. Because of their very low mass and low mechanical frequency in the MHz range, such resonators are highly susceptible to radiation pressure. Moreover, they are good candidates to achieve hybrid optoelectromechanical transducers[14,15] because the out-of-plane vibrational modes of a suspended PCS can be simultaneously coupled with a nearby interdigitated capacitor. Such a device could have a decisive role in future (quantum) information networks because it allows up-conversion of microwave signals onto an optical carrier for subsequent detection or transmission into optical fibers.

---

[1]Laboratoire Kastler Brossel, UPMC-Sorbonne Universités, CNRS, ENS-PSL Research University, Collège de France, 4 place Jussieu, Case 74, F75252 Paris, France; [2]Current address: IBM Research - Zürich, Säumerstrasse 4, 8803 Rüschlikon, Switzerland; [3]Laboratoire de Photonique et de Nanostructures LPN-CNRS/CNRS, Route de Nozay, 91460 Marcoussis, France and [4]Université Paris Diderot, Sorbonne Paris Cité, 75207 Paris, France
Correspondence: T Jacqmin, Email: thibaut.jacqmin@lkb.upmc.fr

Received 23 March 2016; revised 16 June 2016; accepted 13 July 2016; accepted article preview online 18 July 2016

Suspended membranes made from thin layers of high-stress materials are an advantageous platform for the development of optomechanical PCSs because they present excellent mechanical properties[16]. For instance, recent experiments have demonstrated Q-factors exceeding 10^8 with high-stress Si_3N_4 films at room[17,18] and cryogenic[19] temperatures. Moreover, on the optical side, a stringent requirement is the resolved-sideband (or good cavity) limit[20], in which the cavity storage time exceeds the mechanical period. To date, PCS optomechanical resonators have been demonstrated with one-dimensional periodic patterns (often referred to as high-contrast gratings)[11,21] or two-dimensional (2D) photonic-crystal patterns[12,13,18] that are insensitive to the incident polarization and preserve the mechanical stiffness of the membrane. However, in these experiments, the PCS structures suffered from low optical reflectivity, precluding the operation in the resolved-sideband regime, and in most cases, the PCS was fabricated in a low stress material, preventing high mechanical quality factors.

Here we report the implementation and full optical characterization of a 2D PCS directly etched on a high-tensile stress 200 nm-thick Si_3N_4 nanomembrane. We reached the resolved-sideband condition for the first time with a PCS used as the end mirror of a Fabry–Perot cavity. The cavity finesse of 6390 ± 150 is, to the best of our knowledge, an unprecedented value with free-space PCS cavities. The inferred membrane reflectivity is given by $1 - R = 530 \pm 25$ ppm. Moreover, we measured the band diagram of the guided resonances responsible for the Fano resonances in the PCS with an angle-resolved spectrometer. In contrast with previous studies conducted in the context of PCS optical filters[22] and reflectors[23], we give a physical interpretation of the observed band diagram and shed new light on the physics of these structures. Finally, we introduce a theoretical description of the scattering properties of the PCS in the presence of optical losses and demonstrate that the current reflectivity is not limited by material absorption. Demonstrating high-reflectivity PCS in a high-tensile stress film, such as Si_3N_4, as evidenced here could also be beneficial in fields other than optomechanics, such as the generation of tunable optical filters[24] or optomechanical lasers[5].

MATERIALS AND METHODS

Membrane and photonic-crystal fabrication

The commercial membranes[25] are made of a 200-nm stoichiometric Si_3N_4 film deposited on a Si substrate and released over a 1×1 mm square by chemical etching of the substrate (Figure 1a). The high-stress in the film ensures mechanical modes with quality factors as high as 10^8 at low temperature[19] and ultra-low mass[26]. The photonic crystal is realized in the center of the membrane. It is obtained by electron-beam lithography on a layer of 200 nm of polymethyl methacrylate (PMMA) resist, followed by reactive ion etching with a plasma of CHF_3 and SF_6. The PMMA is then stripped off with oxygen plasma. The photonic crystal consists of a 270-μm diameter disk patterned with a square lattice of circular holes (Figure 1). The lattice parameter is $\Lambda = 830$ nm, and the design value for the hole radius is 293 nm.

PCS characterization

Band diagram measurement. We implemented the white-light illumination and imaging setup shown in Figure 2a to measure the PCS band diagram. A white halogen lamp is combined with a set of three lenses (L_1, L_2 and L_3) and two diaphragms (D_1 and D_2) to obtain a Köhler illumination configuration. A field diaphragm (D_1) conjugated to the PCS restricts the illumination to the PCS area, thus reducing the impact of light scattered on the optical elements and mounts. The aperture diaphragm D_2 is used to select the incident beam angles at the PCS position. It is centered on the optical axis, and its aperture width is chosen to reject high angle-of-incidence components that are irrelevant for this experiment. A magnified image of the PCS is obtained with a microscope objective (L_4) and a lens (L_5). A field diaphragm (D_3) sits at the image plane, conjugated to diaphragm D_1, providing additional filtering of unwanted scattered light. A fiber tip is positioned in the focal plane of lens L_6, that is, in the Fourier plane of this imaging system. The light collected by the fiber is guided to a near-infrared spectrometer. By scanning the fiber in the transverse (x, y) plane, the transmission spectrum can be measured at different angles. Moreover, a polarizer (Pol) is introduced between L_1 and L_2 for polarization selection.

PCS reflection, transmission and loss measurements. We implemented a single-ended cavity with the PCS as the end mirror (Figure 2b) to characterize its reflectivity, transmission and losses. The input mirror of the cavity has a 20-mm radius of curvature, and the cavity length is 17.4 mm. This ensures a waist size $w_0 = 48$ μm on the PCS, smaller than the lateral extent of the photonic crystal, and an angular dispersion $\Delta\theta = \arctan\left(\frac{\lambda}{\pi w_0}\right) = 7 \times 10^{-3}$ rad that has a negligible influence on the optical properties of the PCS. A motorized Littman–Metcalf stabilized diode laser system from Sacher Lasertechnik GmbH (Marburg, Germany) (Lion TEC-520) is used to probe the cavity. The cavity transmission is monitored with an avalanche photodiode (Thorlabs, Newton, NJ, USA, APD110C) and is recorded continuously, while the laser wavelength is scanned over 4.8 nm. Simultaneously, the fringes of an imbalanced fiber interferometer are counted by a digital system (based on an Arduino micro-controller[27])

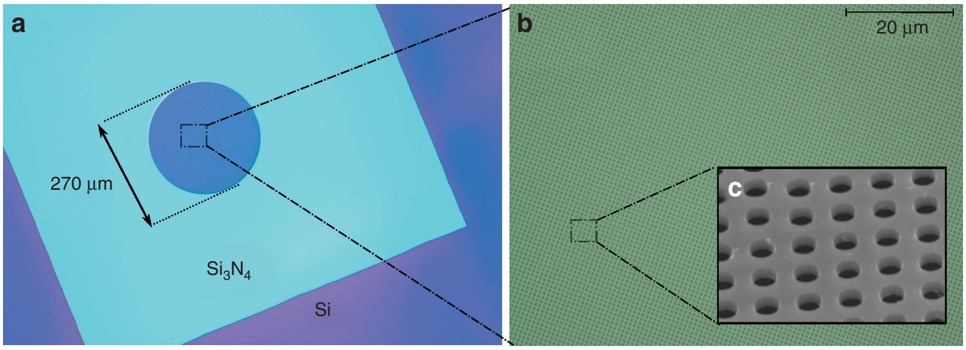

Figure 1 (**a**) Optical image of the PCS made of a high-stress Si_3N_4 membrane suspended on a Si frame. The disk in the center is the photonic crystal. (**b**) Optical microscope image of the PCS. (**c**) Scanning electron micrograph of the PCS.

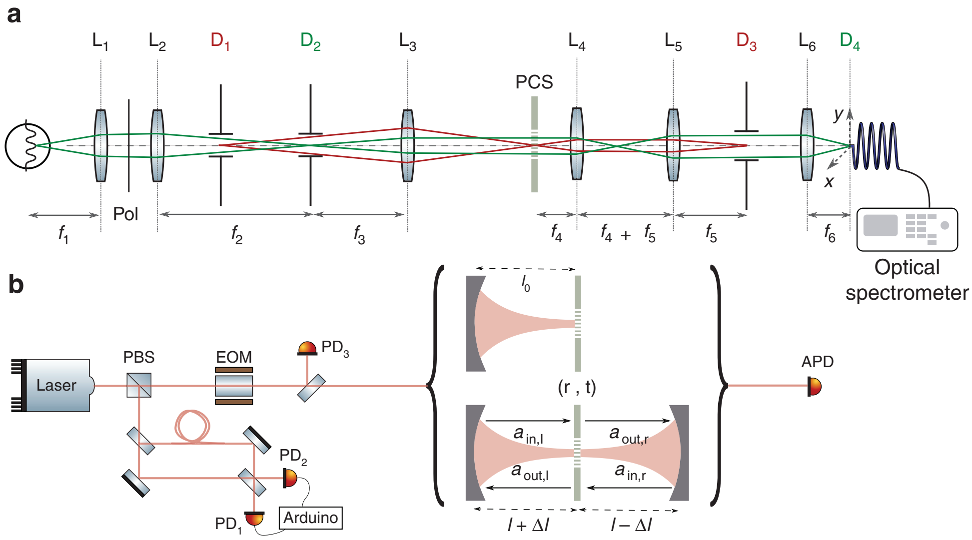

Figure 2 (**a**) Setup used to record the PCS band structure. The light source is a Thorlabs tungsten halogen white lamp (SLS201). The illumination system is made of three lenses (L_1, L_2 and L_3) and two diaphragms (D_1 and D_2). The imaging system is composed of one microscope objective (L_4), two lenses (L_5 and L_6) and two diaphragms (D_3 and D_4). D_4 is a fiber tip that can be scanned along the *x* and *y* directions. Pol is a linear polarizer and PCS is the photonic-crystal sample. The green rays are the Fourier image rays, whereas the red rays are the real image rays. (**b**) Fabry–Perot cavity setups used to measure the membrane reflectivity and losses: the transmission of the cavity is measured by an avalanche photodiode (APD) and is normalized by the incident signal from photodiode PD_3. For the single-ended cavity measurement (top cavity and Figure 4), the laser diode is continuously scanned while an imbalanced interferometer is used to monitor its wavelength (PD_1 and PD_2), and 50 MHz sidebands are generated by an electro-optic modulator (EOM). For the membrane-in-the-middle measurement (bottom cavity and Figure 5), the laser wavelength and membrane positions are scanned by piezoelectric actuators on the grating of the Littman–Metcalf laser system and on the membrane mount, respectively. PBS, polarizing beam splitter.

to measure the laser frequency in real time. The free-spectral range, bandwidth and visibility of each peak are extracted from Lorentzian fits.

Description and characterization of the PCS losses. In the following, we provide a complete theoretical description of the PCS optical properties in the presence of losses. The membrane can be described by its scattering matrix, transforming the fields $a_{\mathrm{in,l}}, a_{\mathrm{in,r}}$ incoming from left and right into outgoing fields $a_{\mathrm{out,l}}, a_{\mathrm{out,r}}$ (Figure 2b):

$$\begin{pmatrix} a_{\mathrm{out,l}} \\ a_{\mathrm{out,r}} \end{pmatrix} = S\cdot\begin{pmatrix} a_{\mathrm{in,l}} \\ a_{\mathrm{in,r}} \end{pmatrix}, \text{with, } S = \begin{pmatrix} r & \bar{t} \\ t & \bar{r} \end{pmatrix} = \begin{pmatrix} r & t \\ t & r \end{pmatrix}$$

where the symmetry of the membrane with respect to the xOy plane is used to assume that the direct (r,t) and reciprocal $(\bar{r},\bar{t})$ complex reflection and transmission coefficients are equal. The previous assumption allows S to be diagonalized

$$S = V\cdot\begin{pmatrix} r+t & 0 \\ 0 & r-t \end{pmatrix}\cdot V^{-1} \tag{1}$$

$$\text{with the change of basis } V = \frac{1}{\sqrt{2}}\begin{pmatrix} 1 & 1 \\ 1 & -1 \end{pmatrix} \tag{2}$$

For a lossless membrane, S is unitary ($|r+t| = |r-t| = 1$), such that within a global phase factor, it is entirely determined by a single real parameter, for instance the transmission intensity $T = |t|^2$. However, in the presence of losses, the scattered fields have a total intensity smaller than the input fields, and both eigenvalues obey

$$|r+t| \leq 1 \tag{3}$$

$$|r-t| \leq 1 \tag{4}$$

Three real parameters (plus a global phase term) are required to fully describe S: in addition to the transmission intensity T, we introduce the optical losses

$$L_{\pm} = 1 - |r \pm t|^2 \tag{5}$$

associated with the symmetric and antisymmetric combinations of the left and right incoming fields $\begin{pmatrix} a_{\mathrm{in,l}} \\ a_{\mathrm{in,r}} \end{pmatrix} \propto \frac{1}{\sqrt{2}}\begin{pmatrix} 1 \\ \pm 1 \end{pmatrix}$. To obtain a measurement of $L_{\pm}$, the membrane can be positioned in the center of a high-finesse cavity. This setup, initially proposed by the group of J. Harris[28], consists of two single-ended cavities coupled via the transmission of the membrane. If the input and output mirrors have the same reflectivity amplitude r' and if both sub-cavities have the same length l, one obtains, in the absence of fields incident from outside the cavity (Figure 2b):

$$a_{\mathrm{in,l}} = tr'e^{-2ikl}a_{\mathrm{in,r}} + rr'e^{-2ikl}a_{\mathrm{in,l}} \tag{6}$$

$$a_{\mathrm{in,r}} = tr'e^{-2ikl}a_{\mathrm{in,l}} + rr'e^{-2ikl}a_{\mathrm{in,r}} \tag{7}$$

where $k = \tilde{\omega}/c$ is the wavenumber of the propagating field. The eigenmodes of the total optical cavity correspond to non-trivial solutions of this system for complex angular frequencies $\tilde{\omega}$. By taking the sum and difference of the previous equations, we obtain

$$a_{\mathrm{in,l}} + a_{\mathrm{in,r}} = (r+t)r'e^{-2ikl}\left[a_{\mathrm{in,l}} + a_{\mathrm{in,r}}\right] \tag{8}$$

$$a_{\mathrm{in,l}} - a_{\mathrm{in,r}} = (r-t)r'e^{-2ikl}\left[a_{\mathrm{in,l}} - a_{\mathrm{in,r}}\right] \tag{9}$$

Non-trivial solutions of this system correspond to symmetric (+) (antisymmetric (−)) modes with angular frequency $\omega_{p,+}$ ($\omega_{p,-}$) and damping (full width at half maximum) γ_+ (γ_-) given by

$$\omega_{p,\pm} = \mathrm{Re}(\tilde{\omega}_{p,\pm}) = -\frac{c}{2l}(\arg[(r \pm t)r'] + 2p\pi) \tag{10}$$

$$\gamma_{\pm} = -2\mathrm{Im}(\tilde{\omega}_{p,\pm}) = -\frac{c}{l}\log(|r \pm t||r'|) \tag{11}$$

where p is an integer corresponding to the longitudinal mode number. From Equation (10), the frequency splitting between the symmetric and antisymmetric modes of identical longitudinal numbers is given by:

$$\Delta\nu = \frac{\omega_{p,+} - \omega_{p,-}}{2\pi} = \frac{c}{4\pi l}\arg\left(\frac{r-t}{r+t}\right) \qquad (12)$$

Finally, if the membrane losses $L_\pm$ and mirror losses $L' = 1 - |r'|^2$ are small, Equation (11) simplifies to

$$\gamma_\pm \approx \frac{c}{2l}(L_\pm + L')$$

Hence, the damping of the symmetric and antisymmetric modes gives direct access to the two parameters L_+ and L_-.

To perform this measurement, a 32-mm long cavity is formed by two mirrors with transmission-limited losses $L' = 455$ ppm and radii of curvature 20 mm. The PCS is set in the center of the cavity on a three-axis translation stage. To align the cavity axis with respect to the PCS, the end mirror is also mounted on a two-axis translation stage. Finally, the PCS frame is glued on a piezoelectric stack to allow automatic scans of its z position over several free spectral ranges.

RESULTS AND DISCUSSION

Band diagram of the PCS

The physics of high-contrast gratings has previously been described in detail[29,30]. Here we extend it to the case of a PCS, following earlier work[13,31]. The high-reflection properties of the PCS result from Fano resonances arising from an interference between the direct reflection from the PCS and light leaking out from internal high-Q guided modes in the PCS. To unveil the band structure of the guided modes, we calculate the transmission of the PCS by rigorous coupled wave analysis (RCWA)[32], which is suitable for periodic structures, such as our square lattice of holes (lattice parameter $\Lambda = 830$ nm, membrane thickness $h = 213$ nm and hole radius $r_h = 276$ nm). We begin the analysis with the unpatterned membrane limit, for which the dielectric constant of both the membrane material and the holes is set to an average value $\varepsilon_{\mathrm{eff}} = \eta\varepsilon_{\mathrm{air}} + (1-\eta)\varepsilon_{\mathrm{Si_3N_4}} = 2.95$. The field solutions are guided modes, referred to as 'unperturbed modes' in the following discussion. They are plane waves reflected by total internal reflection upon the two faces of the membrane. In this regime, the unperturbed modes are evanescent outside of the membrane: the z component of their wavevector fulfils $k_{z,\mathrm{m}} \in \mathcal{R}^+$ inside the membrane and $k_{z,\mathrm{air}} \in i\mathcal{R}^-$ in the surrounding medium. TE (TM) modes have their electric (magnetic) field within the plane of the membrane and are represented in Figure 3 in red (blue). The eight modes are sorted according to their symmetry class with respect to the xOz plane.

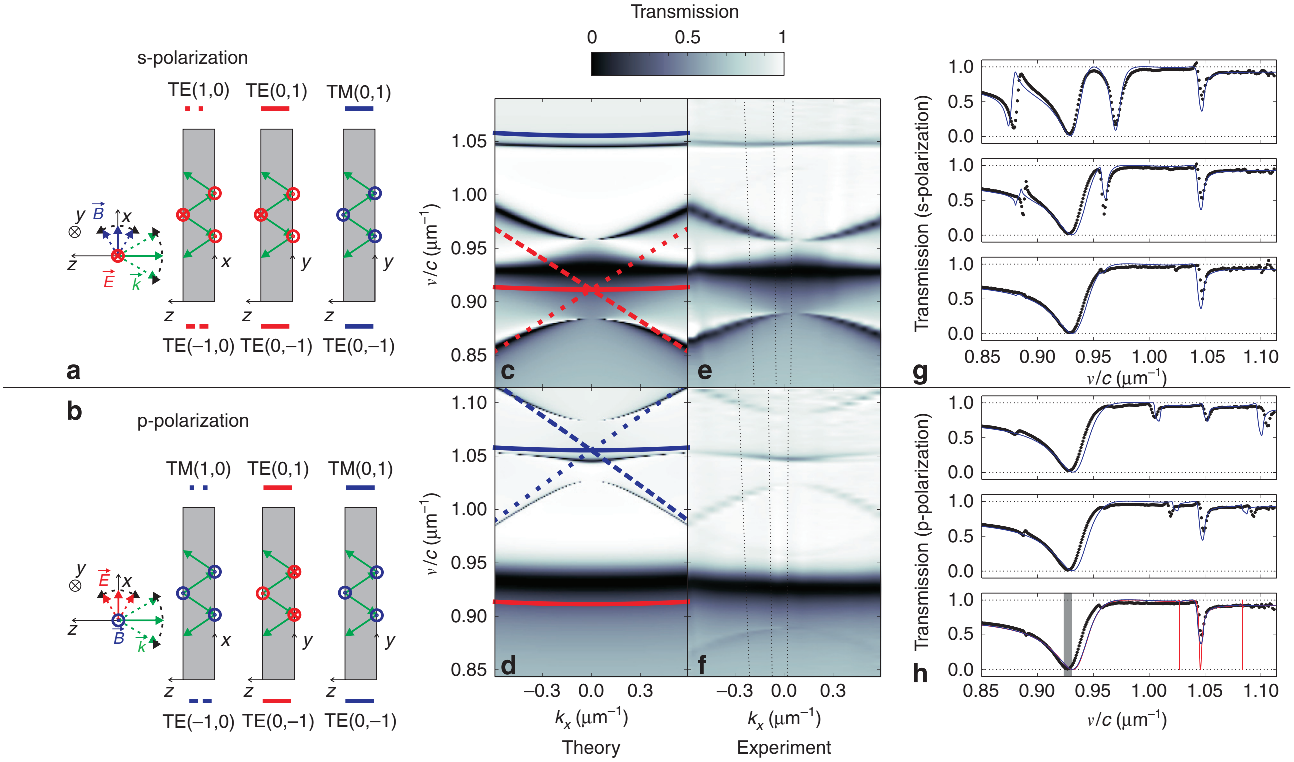

Figure 3 (**a**,**b**) First-order guided modes of an unpatterned membrane illuminated under s-polarization and p-polarization, respectively. (**c**,**d**) Theoretical reflectivity map of a 213-nm-thick PCS patterned with a square lattice of period $\Lambda = 830$ nm, round hole filling factor $\eta = 30.6\%$ and dielectric constant given by[33] $\varepsilon_{\mathrm{Si_3N_4}} = 1 + 2.8939\lambda^2/(\lambda^2 - (0.13867\ \mu\mathrm{m})^2)$, as a function of lateral wavevector k_x, and normalized laser frequency ν/c under s-illumination **c**, and p-illumination **d**. The guided-resonance frequencies of the unpatterned membrane are superimposed, with TE modes in red and TM modes in blue (see **a** and **b** for the list of symbols). (**e**,**f**) Experimental map of the reflectivity measured under s-illumination **e** and p-illumination **f**. (**g**, **h**) Experimental transmission (points) measured for angles of 3.57°, 1.23° and 0.33° (from top to bottom) for s-illumination **g** and p-illumination **h**. The dashed lines of constant $k_x/k_{z,\mathrm{air}}$ in **e** and **f** correspond to these measurements. The corresponding theoretical RCWA fit convoluted with the spectrometer response is plotted as a blue line. As an example, the unconvoluted RCWA result is plotted in red in the last cut of **h**. In this plot, the width of the shaded area corresponds to the wavelength span scanned around the TE resonance in Figure 4.

Symmetric modes (TM($\pm$1, 0)) are not excited under s-illumination, whereas antisymmetric modes (TE($\pm$1, 0)) are not excited under p-illumination. The complex coefficients describing the reflection inside the membrane for the electric field are given by Fresnel's law

$$r_{\mathrm{TM}} = \frac{k_{z,\mathrm{m}} - \varepsilon_{\mathrm{eff}} k_{z,\mathrm{air}}}{k_{z,\mathrm{m}} + \varepsilon_{\mathrm{eff}} k_{z,\mathrm{air}}}, \qquad r_{\mathrm{TE}} = \frac{k_{z,\mathrm{air}} - k_{z,\mathrm{m}}}{k_{z,\mathrm{m}} + k_{z,\mathrm{air}}}$$

We have numerically solved the round-trip resonance condition within the membrane

$$r_j{}^2 e^{-2ik_{z,m}h} = 1 \tag{13}$$

for j = TE or TM and for the lowest possible value of $\omega = c\sqrt{(k_x + 2p_x\pi/\Lambda)^2 + (2p_y\pi/\Lambda)^2 + k_{z,\mathrm{m}}{}^2}$, (where $(p_x, p_y) = (\pm 1, 0)$ or $(p_x, p_y) = (0, \pm 1)$ are the diffraction orders in the x and y directions, respectively). Note that the periodicity Λ is not a property of the unpatterned membrane and is arbitrarily chosen to match that of the patterned membrane. Given the phases of r_{TE} and r_{TM}, we find that TE modes have a lower fundamental resonance frequency than TM modes. Finally, the symmetry of the mode with respect to the xOy plane is given by the sign of the half round-trip propagation coefficient

$$r_j e^{-ik_{z,\mathrm{m}}h} = \pm 1 \tag{14}$$

From the expressions of r_{TE} and r_{TM}, it follows that the fundamental TE (TM) mode is antisymmetric (symmetric) with respect to xOy. The calculated mode frequencies as a function of transverse wavevector k_x are represented by the lines in Figure 3c and 3d. To first order, the frequency of the modes diffracted along the y direction is not affected by the transverse k_x component, contrary to the modes diffracted along the x direction.

The results of the RCWA for the patterned membrane are superimposed as a color plot in Figure 3c and 3d (the refractive index of Si_3N_4 is given by[33] $\varepsilon_{\mathrm{Si_3N_4}} = 1 + 2.8939\lambda^2/(\lambda^2 - (0.13867\ \mu\mathrm{m})^2)$). In this case, the modes described in the unpatterned case are now coupled by diffraction, giving rise to avoided crossings. In addition, the reflections at the membrane/air interfaces couple the guided modes to the zeroth-order modes propagating in free-space, leading to an effective loss channel. The guided resonances acquire a finite lifetime inversely proportional to the width of the Fano resonance (cut along a fixed value of k_x in Figure 3). The lifetime of the TM modes is ~20 times that of the TE modes. At normal incidence, the yOz plane constitutes an additional plane of symmetry (antisymmetry) in the s- (p-) polarization, and, hence, only the combinations TE(1, 0)+TE(−1, 0) and TM (0,1)+TM(0, −1) (respective TE(0, 1)+TE (0, −1) and TM(1, 0)+TM(−1, 0)) are effectively coupled to free-space modes: the linewidth of the other Fano resonances vanishes close to $k_x = 0$. The white-light angle-resolved spectrometer described previously allowed us to measure the band structure of the guided modes for small transverse wavevectors k_x. The experimental transmission with s- (p-) illumination is presented in Figure 3e and 3f, together with three different cuts with incidence angles 3.57°, 1.23° and 0.33°. The simulation is fitted to the data with the hole radius and membrane thickness as free parameters. The former is only specified to within 10% accuracy, and the latter may differ from the design value due to imperfect pattern transfer on electron-beam lithography and etching. The fitted values $r_{\mathrm{h}} = 276$ nm and $h = 213$ nm are in good agreement with the design values. The theoretical fits are represented in blue in Figure 3g and 3h. The reduced visibility of the peaks, particularly pronounced with the TM modes, is accounted for by convolving the theoretical map with the 4-nm wide response of the spectrometer. In the next section, we analyze in greater detail the TE Fano resonance responsible for the largest dip in transmission close to $\nu = c \times 0.929\ \mu\mathrm{m}^{-1} = c/(1.076\ \mu\mathrm{m})$ in Figure 3g and 3h.

Detailed characterization of a Fano resonance

For optical frequencies $\nu = c/\lambda$ close to a guided mode resonance, the PCS complex reflection and transmission coefficients r and t are given in good approximation by the simple two-mode model[31]

$$r(\lambda) = r_d \pm \frac{\gamma}{i(\lambda - \lambda_0) + \gamma}(\pm r_d - t_d) \tag{15}$$

$$t(\lambda) = t_d + \frac{\gamma}{i(\lambda - \lambda_0) + \gamma}(\pm r_d - t_d) \tag{16}$$

where r_d and t_d are the off-resonant coefficients ($|r_d + t_d| = |r_d - t_d| = 1$), λ_0 is the wavelength of the guided mode resonance, γ is the resonance width and the plus/minus sign in Equation (15) reflects the symmetry of the guided mode: as discussed in the previous section, the lowest-order TE mode is antisymmetric with respect to the xOy plane; thus, the minus sign applies. In the absence of optical losses, a striking feature of this Fano lineshape is the existence of a frequency $\lambda_1 = \lambda_0 + i\gamma r_d/t_d$ for which the PCS transmission vanishes: $T(\lambda_1) = |t(\lambda_1)|^2 = 0$, and, accordingly, the reflectivity tends to unity: $R(\lambda_1) = |r(\lambda_1)|^2 = 1$.

By fitting the RCWA results with Equations (15) and (16) around the largest TE Fano resonance, we determine $\lambda_1 = 1076$ nm and $\gamma = 12$ nm. To study the optical behavior of the PCS around λ_1, a single-ended optical cavity of length l_0 is achieved, using the PCS as the end mirror (Figure 2). The transmission of the cavity is monitored, whereas a tunable diode laser is swept across the Fano resonance. The recorded signal, shown in Figure 4a, displays a comb of peaks spaced by the free-spectral range of the cavity given by

$$\Delta\lambda_{\mathrm{FSR}} = \frac{\lambda_0{}^2}{2l_0} \tag{17}$$

The linewidth $\Delta\lambda_n(\lambda)$ of each longitudinal cavity mode n is then obtained by fitting a Lorentzian profile to each of the individual peaks. To minimize the impact of scan-speed fluctuations, we generate 50 MHz sidebands in the laser spectrum with an electro-optic modulator for frequency calibration of the instantaneous scanning speed. Denoting the finesse of the cavity by $F(\lambda)$, the total round-trip loss of the cavity is given by $\Gamma_{\mathrm{RTL}}(\lambda) = 2\pi/F(\lambda) = 2\pi\Delta\lambda_n(\lambda)/\Delta\lambda_{\mathrm{FSR}}(\lambda)$. The results are plotted in blue in Figure 4b as a function of the laser wavelength. The lowest level of $\Gamma_{\mathrm{RTL}} = (985 \pm 25)$ ppm, corresponding to a finesse of 6385 ± 25 was found at $\lambda_1 = 1070.9$ nm. The 5.1 nm discrepancy with respect to the results of Figure 3 is quite small considering that two different membranes from the same microfabrication run were used in these experiments. In the simulations, it is accounted for by changing the hole radius from $r_{\mathrm{h}} = 276$ nm to $r_{\mathrm{h}} = 285$ nm. Taking into account the 455 ppm transmission of the input mirror, we infer a membrane reflectivity as good as $1 - R(\lambda_1) = 530$ ppm.

To discriminate between the contributions of the membrane transmission $T(\lambda) = |t(\lambda)|^2$ and the optical losses $L(\lambda) = 1 - R(\lambda) - T(\lambda)$ in $\Gamma_{\mathrm{RTL}}(\lambda)$, we use the extra information embedded in the height of the transmitted peaks. The transmission $\mathcal{T}_n(\lambda)$ of the cavity at resonance with the nth mode is given by

$$\mathcal{T}_n(\lambda) = \frac{4T_{\mathrm{c}}T(\lambda)}{\Gamma_{\mathrm{RTL}}(\lambda)^2} \tag{18}$$

where T_{c} is the transmission of the input mirror, assumed to be constant over the wavelength range scanned here. In the experiment, a

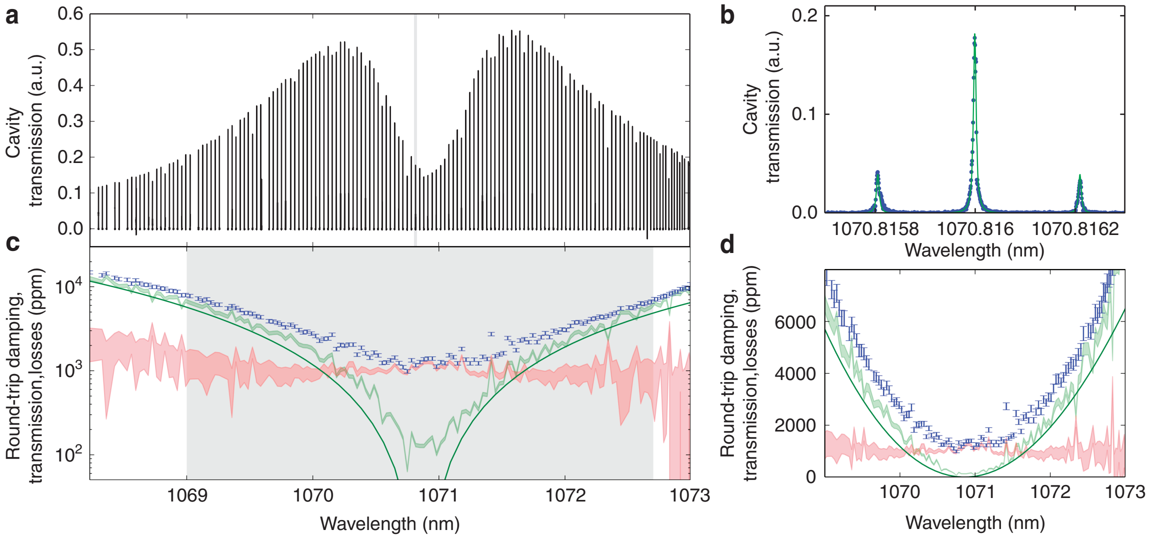

Figure 4 (**a**) Transmission of a single-ended cavity as a function of the laser wavelength. (**b**) Magnification of an individual Airy peak, showing modulation sidebands and a Lorentzian fit. (**c**) Round-trip loss inferred from the fits of individual Airy peaks is shown in blue. The error bars are extracted from the average off-centering of the central peak between the left and right sidebands. The red- and green-shaded areas represent the confidence intervals for the PCS loss and transmission, respectively. The green line is the theoretical transmission calculated by RCWA with the same parameters as Figure 3, except for $r_h = 285$ nm (this experiment uses a second membrane from the same microfabrication run). (**d**) Linear representation of the data in **c**.

signal proportional to $T_n(\lambda)$ is measured, so that we can deduce $\mathcal{T}(\lambda)$ from Equation (18) within a multiplicative constant α. By assuming that the losses $L(\lambda)$ are within the interval $[0, \Gamma_{\mathrm{RTL}}(\lambda_1)]$ at the highest accessible wavelength, we obtain a confidence interval for α and hence for $T(\lambda) = \Gamma_{\mathrm{RTL}}(\lambda) - L(\lambda)$ (in green in Figure 4c and 4d) and $L(\lambda)$ (in red) over the whole wavelength range. For comparison, the transmission calculated by RCWA is displayed by a green solid line in Figure 4c and 4d. The agreement between RCWA and the experimental results is excellent. At the Fano resonance $\lambda_1 = 1070.9$ nm, the round-trip damping is vastly dominated by membrane losses. The lowest cavity bandwidth $\kappa/2 = c/4l_0F(\lambda_1) = 675$ kHz measured in this single-ended cavity setup approaches the resolved-sideband condition for the first-order flexure modes of the suspended membrane.

To understand the exact form of the scattering matrix and to gain insight into the origin of the losses observed in the previous experiment, a PCS is positioned in the middle of a high-finesse cavity. The PCS position Δl is scanned along the cavity axis with a piezoelectric actuator. In this configuration, the PCS couples two cavities of length $l_1 + \Delta l/2$ and $l_2 - \Delta l/2$, where $l_1 \approx l_2 \approx l$ are the initial lengths of the first and second sub-cavities, which are assumed to be simultaneously resonant with the central laser wavelength λ_c for $\Delta l = 0$. The cavity transmission, recorded as a function of Δl and laser detuning $\Delta\nu \propto \lambda_c - \lambda$, is represented in the color plots of Figure 5a–5c. The avoided crossing of the symmetric and antisymmetric modes is visible in the center of the figure. From a Lorentzian fit of the peaks at the avoided crossing and along the vertical axis, we extract the frequency spacing $\Delta\nu$, and the linewidth $\gamma_\pm$ of the symmetric and antisymmetric modes. The experiment is then reproduced for several laser wavelengths λ_c close to the Fano resonance, and the corresponding frequency spacings and linewidths are shown in Figure 5d and 5e, respectively.

In Figure 5a and 5c, the upper and lower branches of the avoided crossing are strongly asymmetric. This is a direct consequence of the difference between L_+ and L_-. For $\lambda_c < \lambda_1$ (Figure 5a), the phase of $(r-t)/(r+t)$ is positive, such that from Equation (12), the symmetric mode (angular frequency ω_+) constitutes the upper branch of the crossing, whereas the antisymmetric mode (angular frequency ω_-) is the lower branch. On the other hand, for $\lambda_c > \lambda_1$ (Figure 5c), $\Delta\nu = (\omega_+ - \omega_-)/2\pi$ changes its sign and the upper and lower branches are exchanged. Finally, at the Fano resonance $\lambda_c = \lambda_1$, r and t are in phase, so the symmetric and antisymmetric modes are perfectly degenerate. Combined with the inequalities of Equation (3), an upper bound for the transmission of the membrane can be derived: $|t| \leq 1 - |r|$ at the Fano resonance. For $1 - R = 985$ ppm, this corresponds to a transmission as low as $T \leq 0.2$ ppm. Hence, the residual transmission of 100 ppm observed in Figure 4 is in contradiction with the two-port description developed in this work. A first explanation is the possible scattering into non-overlapping spatial modes due to surface roughness. Moreover, given our experimental parameters, we expect from RCWA that the wavevector components of the input Gaussian beam not aligned with a symmetry plane of the membrane should give rise to ≈ 20 ppm transmission into the polarization orthogonal to the input beam (with a spatial distribution that is antisymmetric with respect to the xOz and yOz planes). Nevertheless, as shown in Figure 4, the residual transmission only accounts for a small fraction of the total cavity losses close to the Fano resonance, and the nature of these losses remains to be elucidated.

The difference between the losses $L_\pm$ experienced by the symmetric and antisymmetric modes is captured by a simple phenomenological model; because the Fano resonance results from the interference between direct PCS transmission and a high-Q guided resonance, it can be safely assumed that the losses mostly affect the former. Hence, Equations (15) and (16) are modified to include a phenomenological loss rate γ' in the high-Q response as

$$\begin{aligned} r(\lambda) &= r_d + \tfrac{\gamma}{i(\lambda-\lambda_0)+\gamma+\gamma'}(r_d + t_d) \\ t(\lambda) &= t_d - \tfrac{\gamma}{i(\lambda-\lambda_0)+\gamma+\gamma'}(r_d + t_d) \end{aligned}$$

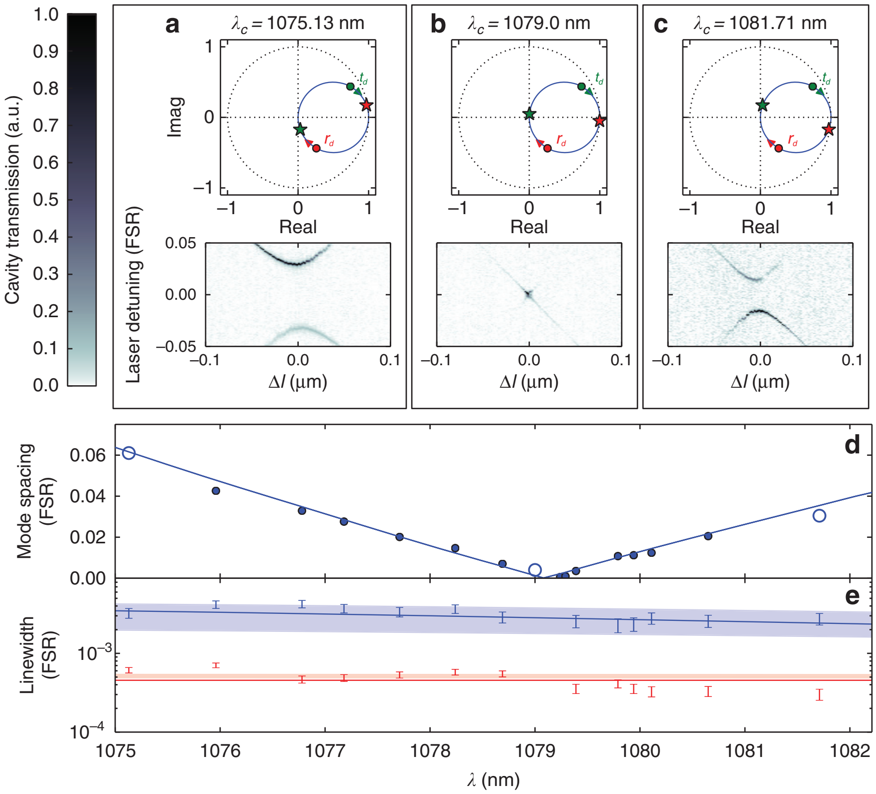

Figure 5 (**a**–**c**) Color plots of the cavity transmission versus the cavity length and laser detuning with respect to three different laser central wavelengths λ_c. Above are the corresponding complex representations of $r(\lambda)$ and $t(\lambda)$, where a global phase factor has been applied to ensure that $r(\lambda_1) = r_d + t_d = 1$. The green and red bullets correspond to $r(\lambda_0) = t_d$ and $t(\lambda_0) = r_d$ respectively, the green and red stars correspond to $t(\lambda_c)$ and $r(\lambda_c)$, respectively. In **a** (**c**), λ_c is chosen smaller (larger) than λ_1. In **b**, λ_c is chosen very close to λ_1 so that $r(\lambda_c) \approx 1$ and $t(\lambda_c) \approx 0$. (**d**) Mode frequency spacing for $\Delta l = 0$. A minimum is reached for $\lambda = \lambda_1$. The blue line corresponds to the mode spacing calculated by RCWA using Equation (12) (same parameters as in Figures 3 and 4, except for $r_h = 272$ nm). (**e**) Linewidths of the two modes. The blue strip represents the value obtained by RCWA simulations, including an absorption of $2 \times 10^{-5} \leq \mathrm{Im}(n) \leq 5 \times 10^{-5}$. Optical detunings are normalized by the FSR of the sub-cavities $\Delta\lambda_{\mathrm{FSR}} = \lambda_c{}^2/2l$. The error bars are inferred from the variation of the fit parameters obtained with neighboring values of Δl.

Using this model, it follows that

$$L_+ = 0 \tag{19}$$

$$L_- = \frac{4\gamma\gamma'}{(\gamma + \gamma')^2 + (\lambda - \lambda_0)^2} \tag{20}$$

thus, only the antisymmetric mode of the two-cavity setup is affected by the optical losses, with a value proportional to the Lorentzian response of the guided resonance. This is an intuitive result because the antisymmetric guided resonance under study is not driven by a symmetric incoming field (and vice versa for the symmetric TM resonance). To quantitatively evaluate the model, Figure 5e shows the total expected losses $L_\pm + L'$, where $\gamma' = 1.0 \times 10^{-2}$ nm is the only adjustable parameter because $\lambda_1 = 1079.1$ nm, $\gamma = 12$ nm and $L' = 455$ ppm are independently determined. Therefore, optical losses are found to account for $<1‰$ of the total decay rate of the guided mode resonance. The previous model shows that the asymmetry between L_+ and L_- is a direct consequence of the physics of Fano resonances and is not specific to a particular loss mechanism, such as absorption or scattering, because both would preferentially affect the high-Q guided mode. This finding is in stark contrast with a model recently proposed in Ref. 21, where such an asymmetry was attributed to absorption in the material. Moreover, we show in the following that absorption should have a negligible influence on the optical loss of our PCS. If the losses observed in our experiment were entirely due to optical absorption, the value $\mathrm{Im}(n) = (3.5 \pm 1.5) \times 10^{-5}$ could be derived for the absorption of the Si_3N_4 layer. The values of $L_\pm + L'$ obtained by RCWA simulation, including an absorption of $2 \times 10^{-5} \leq \mathrm{Im}(n) \leq 5 \times 10^{-5}$ are located within the shaded areas in Figure 5e. Because previous experiments[34] have found values for the absorption of a similar layer that are an order of magnitude smaller ($\mathrm{Im}(n) = 2.0 \times 10^{-6}$), we conclude that scattering is the main source of losses. In the single-ended cavity case, where the field is essentially incident on one side of the membrane, the relevant optical losses are given by $L = (L_+ + L_-)/2$. Thus, the decrease of optical losses with optical wavelength visible in Figure 4b is consistent with Equations (19) and (20). With the previous smaller value of Si_3N_4 absorption, RCWA simulation shows that a reflectivity as high as $R \approx 1 - 80$ ppm, corresponding to a finesse close to 80 000, could be achieved by improving the PCS fabrication process.

CONCLUSIONS

High-stress Si_3N_4 films have been successfully patterned to achieve a 2D PCS and have provided a detailed study of the rich mode structure underlying the high reflectivity of the crystal. We have fully characterized the scattering and loss properties of the device. We have also experimentally demonstrated the wide tunability of the membrane reflectivity via adjustment of the laser wavelength close to a Fano resonance. Such tunability is highly desirable in the context of membrane-in-the-middle optomechanics experiments. In particular, the ability to reach a very narrow energy gap between the eigenmodes of the coupled cavities can be used to enter the regime where the photon exchange time becomes comparable to the mechanical period. This would enable the observation of mechanically induced coherent photon dynamics, such as Autler–Townes splitting or Landau–Zener–Stueckelberg dynamics[35]. Finally, the bandwidth of the single-ended cavity described in this work, as low as 675 kHz, is in the resolved sideband regime for the first-order harmonics of the drum mode, ranging from 596 kHz for the (0, 1) mode to 1.2 MHz for the (2, 2) mode used in previous quantum optomechanics experiments[16]. Hence, this technique results in devices suitable for the development of optomechanical transducers.

ACKNOWLEDGEMENTS

We acknowledge M Corcos, I Krasnokutska, X Pennehouat and L Pinol for preliminary experimental developments. We thank J Palomo and M Rosticher for developing the first steps of the microfabrication process. Finally, we thank J Lawall and R Guérout for insightful scientific discussions. This research has been partially funded by the Agence Nationale de la Recherche programs ‘ANR-2011-BS04-029 MiNOToRe’ and ‘ANR-14-CE26-0002 QuNaT’, the Marie Curie Initial Training Network ‘cQOM’, and the DIM nano-K Ile-de-France program ‘NanoMecAtom’. SC is supported by the Marie Sklodowska-Curie Individual Fellowship program, XC is supported by a fellowship 'Research in Paris' from the city of Paris.

---

1 Zhou WD, Zhao DY, Shuai YC, Yang HJ, Chuwongin S *et al.* Progress in 2D photonic crystal Fano resonance photonics. *Prog Quantum Electron* 2014; **38**: 1–74.
2 Lin CC, Lu ZL, Shi SY, Jin G, Prather DW. Experimentally demonstrated filters based on guided resonance of photonic-crystal films. *Appl Phys Lett* 2005; **87**: 091102.
3 Yacomotti AM, Raineri F, Vecchi G, Monnier P, Raj R *et al.* All-optical bistable band-edge Bloch modes in a two-dimensional photonic crystal. *Appl Phys Lett* 2006; **88**: 231107.
4 Magnusson R, Wawro D, Zimmerman S, Ding YW. Resonant photonic biosensors with polarization-based multiparametric discrimination in each channel. *Sensors* 2011; **11**: 1476–1488.
5 Yang WJ, Adair Gerke S, Wei Ng K, Rao Y, Chase C *et al.* Laser optomechanics. *Sci Rep* 2015; **5**: 13700.
6 Yanik MF, Fan SH. Stopping and storing light coherently. *Phys Rev A* 2005; **71**: 013803.
7 Yacomotti AM, Monnier P, Raineri F, Ben Bakir B, Seassal C *et al.* Fast thermo-optical excitability in a two-dimensional photonic crystal. *Phys Rev Lett* 2006; **97**: 143904.
8 Friedrich D, Barr BW, Brückner F, Hild S, Nelson J *et al.* Waveguide grating mirror in a fully suspended 10 meter Fabry-Perot cavity. *Opt Express* 2011; **19**: 14955–14963.
9 Gavartin E, Braive R, Sagnes I, Arcizet O, Beveratos A *et al.* Optomechanical coupling in a two-dimensional photonic crystal defect cavity. *Phys Rev Lett* 2011; **106**: 203902.
10 Alegre TPM, Safavi-Naeini A, Winger M, Painter O. Quasi-two-dimensional optomechanical crystals with a complete phononic bandgap. *Opt Express* 2011; **19**: 5658–5669.
11 Kemiktarak U, Metcalfe M, Durand M, Lawall J. Mechanically compliant grating reflectors for optomechanics. *Appl Phys Lett* 2012; **100**: 061124.
12 Bui CH, Zheng JJ, Hoch SW, Lee LYT, Harris JGE *et al.* High-reflectivity, high-Q micromechanical membranes via guided resonances for enhanced optomechanical coupling. *Appl Phys Lett* 2012; **100**: 021110.
13 Makles K, Antoni T, Kuhn AG, Deléglise S, Briant T *et al.* 2D photonic-crystal optomechanical nanoresonator. *Opt Lett* 2015; **40**: 174–177.
14 Andrews RW, Peterson RW, Purdy TP, Cicak K, Simmonds RW *et al.* Bidirectional and efficient conversion between microwave and optical light. *Nat Phys* 2014; **10**: 321–326.
15 Bagci T, Simonsen A, Schmid S, Villanueva LG, Zeuthen E *et al.* Optical detection of radio waves through a nanomechanical transducer. *Nature* 2014; **507**: 81–85.
16 Purdy TP, Peterson RW, Regal CA. Observation of radiation pressure shot noise on a macroscopic object. *Science* 2013; **339**: 801–804.
17 Reinhardt C, Müller T, Bourassa A, Sankey JC. Ultralow-noise SiN trampoline MEMS for sensing and optomechanics. *Phys Rev X* 2016; **6**: 021001.
18 Norte RA, Moura JP, Gröblacher S. Mechanical resonators for quantum optomechanics experiments at room temperature. *Phys Rev Lett* 2016; **116**: 147202.
19 Yuan MY, Cohen MA, Steele GA. Silicon nitride membrane resonators at millikelvin temperatures with quality factors exceeding 10^8. *Appl Phys Lett* 2015; **107**: 263501.
20 Schliesser A, Rivière R, Anetsberger G, Arcizet O, Kippenberg TJ. Resolved-sideband cooling of a micromechanical oscillator. *Nat Phys* 2008; **4**: 415–419.
21 Stambaugh C, Xu HT, Kemiktarak U, Taylor J, Lawall J. From membrane-in-the-middle to mirror-in-the-middle with a high-reflectivity sub-wavelength grating. *Annal Phys* 2015; **527**: 81–88.
22 Qiang ZX, Chen L, Yang HJ, Pang HQ, Ma ZQ *et al.* Fano filter modal analysis based on transferred silicon nanomembranes on plastic substrates. *Appl Phys Lett* 2008; **93**: 061106.
23 Singh Chadha A, Zhao DY, Chuwongin S, Ma ZQ, Zhou WD. Polarization- and angle-dependent characteristics in two dimensional photonic crystal membrane reflectors. *Appl Phys Lett* 2013; **103**: 211107.
24 Stomeo T, Grande M, Rainò G, Passaseo A, D’Orazio A *et al.* Optical filter based on two coupled PhC GaAs-membranes. *Opt Lett* 2010; **35**: 411–413.
25 Norcada Inc., Edmonton, AB, Canada. Available at http://www.norcada.com.
26 Purdy TP, Peterson RW, Yu PL, Regal CA. Cavity optomechanics with Si_3N_4 membranes at cryogenic temperatures. *New J Phys* 2012; **14**: 115021.
27 Arduino. Available at http://www.arduino.cc.
28 Thompson JD, Zwickl BM, Jayich AM, Marquardt F, Girvin SM *et al.* Strong dispersive coupling of a high-finesse cavity to a micromechanical membrane. *Nature* 2008; **452**: 72–75.
29 Karagodsky V, Sedgwick FG, Chang-Hasnain CJ. Theoretical analysis of subwavelength high contrast grating reflectors. *Opt Express* 2010; **18**: 16973–16988.
30 Karagodsky V, Chang-Hasnain CJ. Physics of near-wavelength high contrast gratings. *Opt Express* 2012; **20**: 10888–10895.
31 Fan SH, Joannopoulos JD. Analysis of guided resonances in photonic crystal slabs. *Phys Rev B* 2002; **65**: 235112.
32 Liu V, Fan SH. S4: A free electromagnetic solver for layered periodic structures. *Comp Phys Commun* 2012; **183**: 2233–2244.
33 Philipp HR. Optical properties of silicon nitride. *J Electrochem Soc* 1973; **120**: 295–300.
34 Serra E, Bawaj M, Borrielli A, Di Giuseppe G, Forte S *et al.* Microfabrication of large area high stress silicon nitride membranes for optomechanical applications. *AIP Adv* 2016; **6**: 065004.
35 Heinrich G, Harris JGE, Marquardt F. Photon shuttle: Landau-Zener-Stückelberg dynamics in an optomechanical system. *Phys Rev A* 2010; **81**: 011801.